



# Dynamic Guidance of Gliders in Planetary Atmospheres

Rui Dilão<sup>1</sup> and João Fonseca<sup>2</sup>

**Abstract:** Using dynamical systems techniques, a new algorithm to direct the trajectory of gliders to a preassigned target point is proposed. The algorithm is applicable to any unpowered lift-enabled vehicle (glider) traveling in planetary atmospheres, locally determining the shortest path to the target point. The guidance commands are chosen taking into account the drag and lift coefficients of the glider, with a parameterization based on wind tunnel data. As a proof of concept, the new algorithm has been applied to the guidance of the Space Shuttle during its return flight to Earth. Numerical simulations over a wide range of parameter values have shown that the algorithm is resilient to changes in both the initial conditions and the atmospheric conditions. For a typical gliding flight in the Earth's atmosphere, from an altitude of 30 km down to 3 km, the margin of error for reaching the target ranges from 20 to 80 m. DOI: 10.1061/(ASCE)AS.1943-5525.0000499. © 2015 American Society of Civil Engineers.

**Author keywords:** Dynamic guidance; Navigation; Planetary atmosphere; Aerodynamics; Glider; Space Shuttle.

## Introduction

While returning from space, spacecraft travel at extreme conditions of speed and acceleration, forcing, at least partially, the automation of the flight controls. For the Space Shuttle, a typical return flight (from space to Earth) has four main phases:

1. The reentry burn, where the effect of atmosphere is negligible and the glider decreases its speed. The glider leaves the orbital level of the International Space Station (ISS) and initiates the reentry burn using nose thrusters to reduce orbital speed. Typical altitudes for this phase are in the 370–120 km range.
2. The atmospheric reentry phase, where the transition from spacecraft to glider is operated. Typical altitudes for this phase are in the 120–40 km range.
3. The gliding phase, where the aerodynamic forces become strong enough to be used to control the glider. Typical altitudes for this phase are in the 40–3 km range.
4. The final approach and landing phase, which is typically initiated at an altitude of 3 km and finishes with the runway touchdown.

During the atmospheric reentry phase, the main priority of the guidance system is to choose a trajectory that does not exceed the structural limits of the glider in terms of heat flux. During the gliding phase, the main priority of the guidance system is to ensure that the glider does not run out of energy before it reaches the location where, with the correct alignment, it can start the final approach and landing. During the gliding section, the structural limits change and the limiting factor is the dynamic pressure on the wings, a pure mechanical force. The final section of the gliding phase starts typically at a speed of Mach 2, at an altitude of around 24 km, and is referred to as terminal area energy management (TAEM). During

TAEM, the glider is guided to the center of the heading alignment circle (HAC) and aligned with the runway, so that the final approach and landing may be initiated.

In the case of the Space Shuttle, the original guidance and control mechanism relied on preprogrammed maneuvers (Harpold and Gavert 1983), calculated from a reference trajectory with a control law based on the linearized flight dynamics (Harpold and Graves 1979). As a result, any errors in the initial conditions of the reentry flight or any unexpected atmospheric profile changes were not dealt with during the automated flight section. To solve this problem, at the end of the TAEM, four different ways of approaching the runway were introduced, translated into four different HACs, to deal with the expected range of energy deviations near the runway (Findlay et al. 1982). Due to technological limitations, at the time the Space Shuttle was built, the end of the TAEM section (near the HAC) was never automated. When subsonic speed was reached, the commander of the glider typically took manual control to execute the alignment with the runway, followed by the final approach and landing. Furthermore, changing the final destination while on flight, necessary in case of emergency, for example, implied loading a complete set of new flight instructions and not simply changing the target coordinates (Findlay et al. 1982).

Approaches different from the original guidance and control mechanism used in the Space Shuttle have been proposed. Some of these approaches were based on precomputed maneuvers (Rehder and Holloway 1972) with hopping across different trajectories (Jiang and Ordonez 2007; Costa 2003; Vernis and Ferreira 2004; Trélat 2002), and relying on heavy computational methods based on shooting techniques to find admissible trajectories (Bonnard et al. 2005; Horneman 2010). Some were limited to straight-line flight paths or assumed an almost horizontal gliding approximation for three dimensional flights (Mease et al. 1999). For practical methods using optimal control, see Betts (1998), Trélat (2012) and Betts (2010). For a recent review of guidance algorithms, see Lu (2014).

In this paper, a new dynamic guidance algorithm is derived, conducting the glider to a target point. This approach is based on dynamical systems techniques that locally determine the shortest feasible path to the target point. The proposed algorithm sequentially selects attack and bank angles, compatible with the aerodynamic characteristics and the structural limits of the glider.

<sup>1</sup>Professor, Dynamical Systems and Mathematical Physics, Non-linear Dynamics Group, Instituto Superior Técnico, Av. Rovisco Pais, 1049-001 Lisbon, Portugal (corresponding author). E-mail: ruidilao@tecnico.ulisboa.pt

<sup>2</sup>Ph.D. Student, Instituto Superior Técnico, Av. Rovisco Pais, 1049-001 Lisbon, Portugal.

Note. This manuscript was submitted on April 4, 2014; approved on January 29, 2015; published online on April 14, 2015. Discussion period open until September 14, 2015; separate discussions must be submitted for individual papers. This paper is part of the *Journal of Aerospace Engineering*, © ASCE, ISSN 0893-1321/04015012(12)/\$25.00.

The proposed algorithm runs iteratively, enabling a self-correcting approach to the target and is applicable to any glider traveling in a planetary atmosphere. The algorithm is computationally fast, enabling the possibility of implementing onboard the automated dynamic guidance of gliders. In addition, the proposed algorithm is extremely resilient to changes in the initial conditions, to changes in the control time interval, and to changes to the atmospheric profiles of air temperature and density, and is also extremely flexible to allow in-flight target coordinate changes. Due to its flexibility and accuracy, it is possible to use the algorithm in a model of a flat Earth, where errors in the localization of faraway targets are dynamically corrected during the approach to the target. The necessary information needed for the implementation of the algorithm is the accurate knowledge of position and attitude parameters of the glider. The physical characteristics of the glider must also be known and coded in its aerodynamic drag and lift coefficients, fitted from wind tunnel data.

For the technical implementation of the model, additional complexity must be taken into account, for example, the introduction of flight instabilities, errors in the navigation, and a full six-degrees-of-freedom model of a rotating Earth (Zipfel 2007).

## Equations of Motion

The motion of a glider in a gravity field without atmosphere can be described by a point-mass model (Miele 1962; Hull 2007; Gallais 2007). The introduction of the atmosphere in the point-mass model induces the aerodynamic forces of drag and lift. The drag force  $D$  acts on the glider parallel to the velocity vector, but in the opposite direction. The lift force  $L$  is perpendicular to the velocity vector of

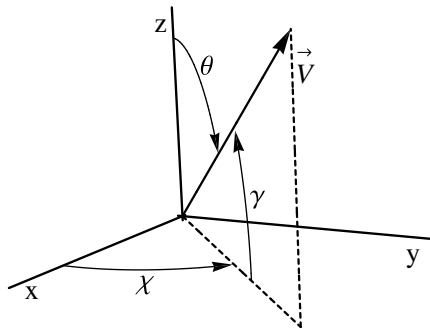


**Fig. 1.** Local coordinate system for the point mass glider model; the origin of the coordinate system is located at the center of mass of the glider;  $\vec{V}$  = glider velocity

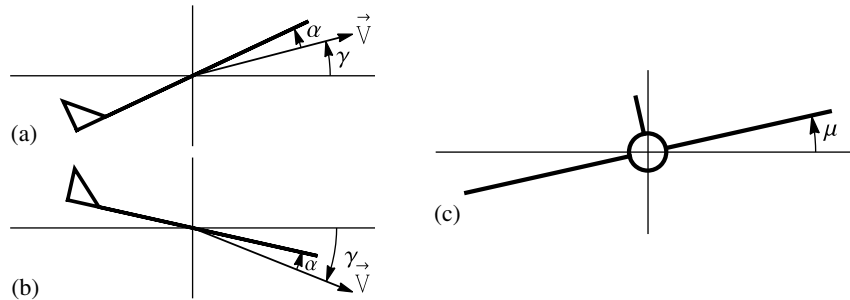


**Fig. 2.** (a and b) Flight descent path angle  $\gamma$  and the angle of attack  $\alpha$  of a glider are shown; (c) bank angle  $\mu$  is shown, measuring the inclination of the glider

the spacecraft and is also perpendicular to the plane of the wings of the aircraft. Under these conditions, the equations of motion of a glider moving in a gravity field and under the influence of the atmosphere are

$$\begin{aligned} m\dot{V} &= -mg(z) \sin \gamma - D(\alpha, M) \\ mV\dot{\gamma} &= -mg(z) \cos \gamma + L(\alpha, M) \cos \mu \\ mV\dot{\chi} \cos \gamma &= L \sin \mu \quad \dot{x} = V \cos \chi \cos \gamma \\ \dot{y} &= V \sin \chi \cos \gamma \quad \dot{z} = V \sin \gamma \end{aligned} \quad (1)$$

where  $g(z)$  = gravity acceleration as a function of height;  $m$  = mass of the glider;  $\gamma$  = flight descent path angle;  $\mu$  = bank angle;  $\alpha$  = angle of attack;  $\theta + \gamma = \pi/2$ ; and  $V^2 = V_x^2 + V_y^2 + V_z^2$ . In the local reference frame of the glider center of mass (Fig. 1),  $V \in ]0, \infty[$ ,  $\gamma \in ]-\pi/2, \pi/2[$ ,  $\chi \in [0, 2\pi[$ ,  $\mu \in ]-\pi/2, \pi/2[$ , and  $\alpha \in ]-\pi/2, \pi/2[$ . The geometric construction of  $\gamma$ ,  $\mu$ , and  $\alpha$  is shown in Figs. 2(a–c). The terms  $D(\alpha, M)$  and  $L(\alpha, M)$  are the drag and the lift forces induced by the effect of the atmosphere, and  $M$  is the Mach number. In general, the Mach number  $M$  is a function of  $V$  and  $z$ . The function  $g(z) = g_0[R_E/(R_E + z)]^2$  is the gravity acceleration, where  $g_0 = 9.80665 \text{ m/s}^2$  is the Earth standard gravitational acceleration constant, and  $R_E = 6.371 \times 10^6 \text{ m}$  is the Earth mean radius. In the reference frame of Fig. 2, positive values of  $\mu$  correspond to left turns and negative values of  $\mu$  correspond to right turns.

The drag and lift forces in the system of Eq. (1) are

$$\begin{aligned} D(\alpha, M) &= \bar{q}SC_D(\alpha, M) = \frac{1}{2}\rho(z)V^2SC_D(\alpha, M) \\ L(\alpha, M) &= \bar{q}SC_L(\alpha, M) = \frac{1}{2}\rho(z)V^2SC_L(\alpha, M) \end{aligned} \quad (2)$$

where  $\bar{q} = \rho(z)V^2/2$  is the dynamic pressure;  $S$  = effective area of the glider corresponding to the combined effect of the wings and the lifting body;  $\rho(z)$  = atmosphere density as a function of the altitude; and  $M$  = Mach number. For each specific glider, the functions  $C_D(\alpha, M)$  and  $C_L(\alpha, M)$  are determined through wind tunnel experiments or computational fluid dynamics (CFD) codes, which explicitly take into account turbulence effects (Raymer 2006).

The Mach number is defined by  $M = V/V_{\text{sound}}$ , where the sound speed  $V_{\text{sound}}$  is calculated through

$$V_{\text{sound}} = \sqrt{\gamma_d R_s T(z)} \quad (3)$$

where  $\gamma_d = 1.4$  = diatomic nonionized gas constant;  $R_s = 287.04 \text{ J/(K kg)}$  = ideal gas constant; and  $T(z)$  = temperature profile of the Earth atmosphere [US Standard Atmosphere (NASA 1976)].

Introducing Eq. (2) into Eq. (1), the final form for the equations of motion of a glider are

$$\begin{aligned}\dot{V} &= -g(z) \sin \gamma - \left[ \frac{1}{2m} \rho(z) S C_D(\alpha, \mathbf{M}) \right] V^2 \\ \dot{\gamma} &= -\frac{g(z)}{V} \cos \gamma + \left[ \frac{1}{2m} \rho(z) S C_L(\alpha, \mathbf{M}) \right] V \cos \mu \\ \dot{\chi} &= \left[ \frac{1}{2m} \rho(z) S C_L(\alpha, \mathbf{M}) \right] V \frac{\sin \mu}{\cos \gamma} \quad \dot{x} = V \cos \chi \cos \gamma \\ \dot{y} &= V \sin \chi \cos \gamma \quad \dot{z} = V \sin \gamma\end{aligned}\quad (4)$$

All the geometric features of the motion of a glider in a planetary atmosphere are described in the six-dimensional phase space of the ordinary differential Eq. (4). However, assuming that  $g$  and  $\rho$  are slow varying functions of the altitude  $z$ , the system of Eq. (4) can be decoupled into two sets of differential equations, one for the attitude of the glider and the other for the three-dimensional spatial position. For low planetary altitudes,  $z \leq 40$  km, the glider will reach a steady state in the attitude variables  $(V, \gamma, \chi)$ . This will enable to design a dynamic guidance algorithm to direct the glider to a target.

### Steady State

The three-dimensional attitude phase space with coordinates  $(V, \gamma, \chi)$  will be called the reduced phase space of the system of Eq. (4). Assuming that  $\rho$ ,  $g$ , and  $\text{Ma}$  are slowly varying functions of  $z$ , a glider under the influence of a gravity field continuously converges to a steady state. The steady state is characterized by a constant velocity, a constant flight descent path angle, and a constant angular speed. The steady state of the attitude equations in Eq. (4) is

$$\begin{aligned}V^* &= \sqrt{\frac{2mg}{\rho S}} \frac{1}{(C_D^2 + C_L^2 \cos^2 \mu)^{1/4}} \\ \gamma^* &= -\arctan \frac{C_D}{C_L \cos \mu} \\ \chi(t) &= \sqrt{\frac{g\rho S}{2m}} (C_D^2 + C_L^2 \cos^2 \mu)^{1/4} \tan \mu + \chi(0) \\ &= \omega^* t + \chi(0) \bmod(2\pi)\end{aligned}\quad (5)$$

where  $\chi(0)$  = initial longitudinal angle;  $\omega^* = g(z) \tan \mu / V^*$  = steady state angular speed;  $C_L \equiv C_L(\alpha, \mathbf{M})$ ;  $C_D \equiv C_D(\alpha, \mathbf{M})$ ;  $\mathbf{M} \equiv \mathbf{M}[V, V_{\text{sound}}(z)]$ ;  $g \equiv g(z)$ ; and  $\rho \equiv \rho(z)$ .

If  $\mu = 0$ , the steady state in Eq. (5) is a fixed point in the three-dimensional reduced phase space with coordinates  $(V, \gamma, \chi)$ . If  $\mu \neq 0$ , the steady state in Eq. (5) is a closed orbit or limit cycle in the three-dimensional reduced phase space  $(V, \gamma, \chi)$ .

In the neighborhood of the steady solution of Eq. (5), the qualitative structure of the vector field of the three-dimensional reduced phase space of the first three equations in Eq. (4) can be analyzed by linearization, obtaining

$$\begin{bmatrix} \dot{V} \\ \dot{\gamma} \\ \dot{\chi} \end{bmatrix} = \begin{bmatrix} \frac{-C_D(\alpha, \mathbf{M}) S \rho(z)}{m} V^* & \frac{-C_L(\alpha, \mathbf{M}) S \rho(z)}{2m} V^{*2} \cos \mu & 0 \\ \frac{C_L(\alpha, \mathbf{M}) S \rho(z)}{m} \cos \mu & \frac{-C_D(\alpha, \mathbf{M}) S \rho(z)}{2m} V^* & 0 \\ \frac{g(z)}{V^{*2}} \tan \mu & \frac{-g(z) C_D(\alpha, \mathbf{M}) \sin \mu}{V^* C_L(\alpha, \mathbf{M}) \cos^2 \mu} & 0 \end{bmatrix} \begin{bmatrix} V \\ \gamma \\ \chi \end{bmatrix}\quad (6)$$

and the matrix in Eq. (6) has eigenvalues

$$\begin{aligned}\lambda_{1,2} &= \frac{S \rho(z)}{4m} V^* [-3C_D(\alpha, \mathbf{M}) \\ &\quad \pm \sqrt{C_D^2(\alpha, \mathbf{M}) - 4C_L^2(\alpha, \mathbf{M})(1 + \cos 2\mu)}] \\ &= \sqrt{\frac{S \rho(z) g(z)}{8m}} \\ &\quad \times \left\{ \frac{-3C_D(\alpha, \mathbf{M}) \pm \sqrt{C_D^2(\alpha, \mathbf{M}) - 4C_L^2(\alpha, \mathbf{M})(1 + \cos 2\mu)}}{[C_D^2(\alpha, \mathbf{M}) + C_L^2(\alpha, \mathbf{M}) \cos^2 \mu]^{1/4}} \right\} \\ \lambda_3 &= 0\end{aligned}\quad (7)$$

The convergence of the glider trajectory to the steady state is determined by the eigenvalues  $\lambda_{1,2}$ . If  $\lambda_{1,2}$  are real, then  $\lambda_{1,2} < 0$ , and the convergence to the steady state is monotonic [in the  $(V, \gamma)$  subspace, the fixed point is a stable node]. If  $\lambda_{1,2}$  are complex,  $\text{Real}(\lambda_{1,2}) < 0$ , and the convergence to the steady state is oscillatory [in the  $(V, \gamma)$  subspace, the fixed point is a stable focus].

In Fig. 3, the reduced phase space orbits of Eq. (4) near the fixed point  $(V^*, \gamma^*)$ , in the plane  $\chi = \text{constant}$ , is shown. These phase spaces orbits have been obtained with the choice of parameters,  $\rho(z) S C_D(\alpha, \mathbf{M}) / (2m) = \rho(z) S C_L(\alpha, \mathbf{M}) / (2m) = 1$ , and  $g = 9.8$ . The bank angle  $\mu$  affects both the position of the fixed point in the phase space and the regime of convergence to the steady state.

### Relaxation Time

In the presence of the atmosphere, where  $\rho(z) > 0$ , and for arbitrary initial conditions in the reduced phase space  $(V, \gamma, \chi)$ , the speed  $V$  of the glider and the flight descent path angle  $\gamma$  tend to the steady state  $(V^*, \gamma^*)$ . Theoretically, the glider takes infinite time to reach the steady state. However, the convergence time to the neighborhood of the steady state in the reduced phase space can be estimated and will be referred to as relaxation time.

The relaxation time is estimated through the linearized Eq. (6). As  $\text{Real}(\lambda_{1,2}) < 0$ , the solutions of Eq. (6) are dominated by the nonzero eigenvalue of Eq. (7) with the largest real part. Let  $\lambda_{\max} = \max[\text{Real}(\lambda_1), \text{Real}(\lambda_2)]$ . Therefore, the approximate displacement of the glider attitude coordinates relative to the steady state  $(V^*, \gamma^*)$  is

$$\begin{aligned}\Delta V(t) &= [V(t) - V^*] \simeq (V_0 - V^*) e^{\lambda_{\max} t} \\ \Delta \gamma(t) &= [\gamma(t) - \gamma^*] \simeq (\gamma_0 - \gamma^*) e^{\lambda_{\max} t}\end{aligned}\quad (8)$$

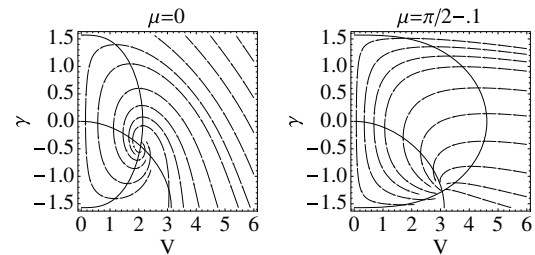


**Fig. 3.** Orbits in the reduced phase space of Eq. (4), in the plane  $\chi = \text{constant}$ , for two values of the bank angle  $\mu$ ; the  $V$  and  $\gamma$  nullclines of Eq. (4) are also shown; for  $\mu = 0$ , the eigenvalues  $\lambda_{1,2}$  are complex and the fixed point is a stable focus in the  $(V, \gamma)$  phase space; for  $\mu = \pi/2 - 0.1$ , the eigenvalues  $\lambda_{1,2}$  are real and the fixed point is a stable node

where  $(V_0, \gamma_0)$  are the initial coordinates of the glider and  $\lambda_m < 0$ . In the reduced phase space with coordinates  $(V, \gamma)$ , near the steady state  $(V^*, \gamma^*)$  the relative distance in phase space from the current position to the steady state  $(V^*, \gamma^*)$  is

$$d_r = \sqrt{\frac{\Delta V(t)^2}{V^{*2}} + \frac{\Delta \gamma(t)^2}{\gamma^{*2}}} \quad (9)$$

where  $d_r \geq 0$ . Let  $d_V^2 = \Delta V(t)^2/V^{*2}$  and  $d_\gamma^2 = \Delta \gamma(t)^2/\gamma^{*2}$ . Assuming that the steady state is reached if  $d_r$  is small, for example  $d_r = 0.1$ , by Eqs. (8) and (9), we have

$$d_r = \sqrt{d_V^2 + d_\gamma^2} = \sqrt{\frac{(V_0 - V^*)^2}{V^{*2}} + \frac{(\gamma_0 - \gamma^*)^2}{\gamma^{*2}}} e^{\lambda_{\max} t} \quad (10)$$

Solving Eq. (10) in order to  $t$ , the glider will be in the vicinity of the steady state after the relaxation time

$$t_r = \frac{1}{\lambda_{\max}} \frac{\log(d_V^2 + d_\gamma^2)}{\log\left[\frac{(V_0 - V^*)^2}{V^{*2}} + \frac{(\gamma_0 - \gamma^*)^2}{\gamma^{*2}}\right]} \quad (11)$$

provided that  $\log(d_V^2 + d_\gamma^2) \leq \log[(V_0 - V^*)^2/V^{*2} + (\gamma_0 - \gamma^*)^2/\gamma^{*2}] := d$ . If  $\log(d_V^2 + d_\gamma^2) > d$ , in line with the initial assumption that when reaching the neighborhood of the fixed point, the glider has already achieved the steady state, it can be assumed that  $t_r = 0$ .

The relaxation time concept will be used as a quantitative measurement of the time left to reach the steady state neighborhood.

**Table 1.** Parameters of the Aerodynamic Drag and Lift Coefficients [Eq. (12)] for the Space Shuttle, Estimated from Wind Tunnel Data

Parameter	Estimated	Standard error	$t$ -statistics	$p$ -value
$a_1$	-0.053	0.009	-6.15	$9.8 \times 10^{-8}$
$a_2$	2.73	0.06	43.0	$1.8 \times 10^{-43}$
$a_3$	-1.55	0.09	-18.0	$2.0 \times 10^{-24}$
$b_1$	-1.01	0.09	-11.3	$7.4 \times 10^{-16}$
$b_2$	1.1	0.1	8.7	$7.6 \times 10^{-12}$
$d_3$	1.79	0.02	99.0	$1.1 \times 10^{-63}$
$e_1$	-1.4	0.1	-12.6	$1.2 \times 10^{-17}$
$e_2$	1.5	0.1	11.3	$5.8 \times 10^{-16}$
$f_1$	0.028	0.004	6.46	$2.9 \times 10^{-8}$
$f_2$	1.4	0.2	8.57	$1.0 \times 10^{-11}$
$M_c$	1.25	0.03	49.6	$1.0 \times 10^{-46}$

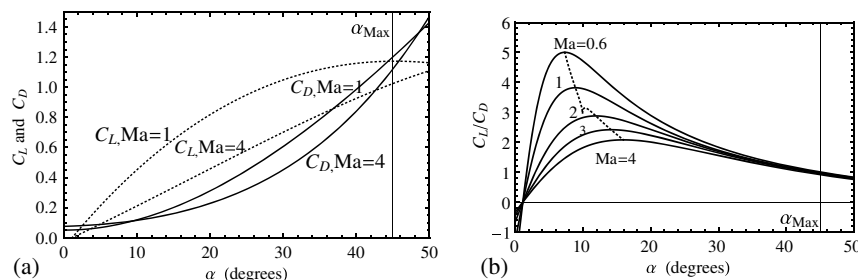


**Fig. 4.** (a) Lift (dotted) and drag coefficients  $C_L$  and  $C_D$  for the Space Shuttle as a function of  $\alpha$ , for several values of the Mach number  $M$ ; these coefficients have been calculated from Eqs. (12) and (13) and the parameters in Table 1; (b) ratio  $L/D$ , as a function of the angle of attack  $\alpha$ , for several values of the Mach number  $Ma$ ; max-glide angle  $\alpha_{\max gl}$  (dotted line) is given by Eq. (14)

## Aerodynamic Coefficients for the Space Shuttle

### Parametrization of the Aerodynamic Coefficients

Using wind tunnel data, the aerodynamic drag and lift coefficients  $C_D$  and  $C_L$  of the Space Shuttle have been fitted with the parameterizations

$$\begin{aligned} C_L(\alpha, M) &= (a_1 + a_2\alpha + a_3\alpha^2)K(M)^{b_1+\alpha b_2} \\ C_D(\alpha, M) &= (0.01 + f_1M^{f_2} + d_3\alpha^2)K(M)^{e_1+\alpha e_2} \end{aligned} \quad (12)$$

where

$$K(M) = \frac{1}{2} \left( 1 + \sqrt{1 - \left( \frac{M}{M_c} \right)^2} \right) \quad (13)$$

is a simplification of the von Kármán function expanded to supersonic regimes (Shevell 1988). In Table 1, the parameter estimations for Eqs. (12) and (13) are shown, based on wind tunnel data from Ramsey (1972). The significance of the fits has been determined with a chi-squared test. The large values of the absolute value of the  $t$ -statistics measures the likelihood of the parameters in the fits. The low values of the  $p$ -values mean that the fits are highly significant and the probability of finding a value outside the fitted ones are in the range  $10^{-8} - 10^{-63}$ .

In Fig. 4(a), the lift and drag coefficients  $C_L$  and  $C_D$  as a function of the attack angle  $\alpha$ , for several values of the Mach number, are shown. In Fig. 4(b), the behavior of the ratio  $L/D$ , as a function of the angle of attack  $\alpha$  is shown. The aerodynamic characteristics of gliders are constrained by its  $L/D = C_L/C_D$  state curve. All the  $L/D$  curves intersect at the no-lift angle  $\alpha_{nL} = 1.5^\circ$ . The no-lift angle  $\alpha_{nL}$  is the angle for which  $L/D$  is zero due the absence of lift force, and is independent of the Mach number. The max-glide angle  $\alpha_{\max gl}$  is the angle that maximizes the ratio  $L/D$ , and depends on the Mach number. The maximum angle of attack  $\alpha_{\max} = 45^\circ$  is the maximum attack angle allowed for the Space Shuttle and is independent of the Mach number.

### Parameterization of the Max-Glide Angle As a Function of the Mach Number

Using Eqs. (12) and (13), the max-glide angle  $\alpha_{\max gl}$  as a function of Mach number can be approximated by the function



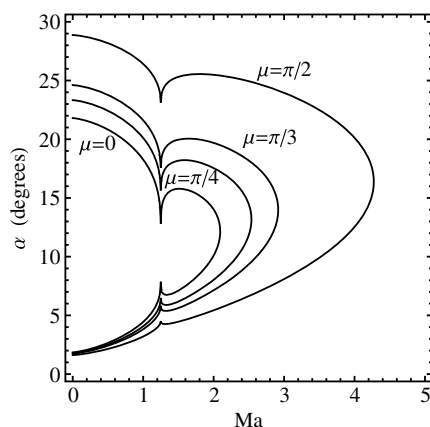


**Fig. 5.** Different convergence regimes for the Space Shuttle as a function of the attack angle  $\alpha$  and the Mach number  $M$ , for different values of  $\mu$ ; in the interior of the corresponding  $\mu$ -curve, the convergence to the steady state is oscillatory; outside of its  $\mu$ -curve the convergence is monotonic

$$\alpha_{\max gl}(M) = \begin{cases} 0.0906 + 0.0573M + 0.0071M^2 & (M \leq 1.25) \\ 0.1070 + 0.0577M - 0.0037M^2 & (1.25 < M < 5) \end{cases} \quad (14)$$

determined with the correlation coefficient  $r^2 = 0.999$ , Fig. 4(b).

Using the aerodynamic coefficients of the Space Shuttle, it is possible to map the different regimes of convergence to the steady state as a function of the attack angle and the speed of the glider, measured in Mach units. These regimes depend on the eigenvalues  $\lambda_{1,2}$ , given in Eq. (7). In Fig. 5, the different convergence regimes for the Space Shuttle as a function of the attack angle and the Mach number are shown. For high Mach numbers, the convergence to the steady motion is non oscillatory, regardless of the attack angle  $\alpha$ .

## Space Shuttle Dynamics in the Earth's Atmosphere

In the high layers of the atmosphere, where the air density is extremely low, a glider does not typically travel in a steady state. However, given enough time, it naturally converges to a steady state (Miele 1962). As, by Eq. (7),  $\lambda_{1,2} \propto 1/\sqrt{\rho(z)}$  and since the air density increases as altitude decreases, by Eq. (11), the relaxation time  $t_r \propto 1/\sqrt{\rho(z)}$  decreases as the glider approaches target points located at lower altitudes. To demonstrate this behavior, several simulations were performed, by numerically integrating Eq. (4) with the drag and lift coefficients of Eqs. (12) and (13). The Earth atmosphere has been simulated using the data in references US Standard Atmosphere (NASA 1976) and Dilão and Fonseca (2013).

In Fig. 6, the time evolution of the vertical position of the glider, its speed, and its flight descent path angle  $\gamma$  as a function to time are shown for the choice  $\alpha = \alpha_{\max gl}$ , where  $\alpha_{\max gl}$  has been calculated by Eq. (14) and the Mach number has been calculated with Eq. (3). The chosen initial conditions for the glider were ( $x_0 = 0$  km,  $y_0 = 0$  km,  $z_0 = 120$  km) and ( $V_0 = 6,500$  m/s,  $\gamma_0 = -2^\circ$ ,  $\chi_0 = 0^\circ$ ). To restrict the flight to the ( $x, z$ ) plane for simplicity, a constant bank angle  $\mu = 0$  has been imposed. From these simulations, it follows that, in the upper layers of the atmosphere ( $z > 40$  km), the speed and the flight descent path angle are not in a steady state. For  $z < 40$  km, the speed and the flight descent path angle approach the steady values  $V^*$  and  $\gamma^*$ . For  $z < 40$  km or  $t > 700$  s, the steady state is reached in speed and in descent path angle  $\gamma$ .

In Fig. 7, the same simulations were performed, with constant attack angle choice  $\alpha = \alpha_{\max} = 45^\circ$ . Again, from these simulations, it follows that for  $z < 40$  km, the speed and the flight descent path angle are increasingly close to the steady values  $V^*$  and  $\gamma^*$ . As in the case of Fig. 6, for  $z < 40$  km or  $t > 500$  s, the steady state in the speed and in the attitude angle  $\gamma$  is reached. This behavior is independent of the choices made on the attack angle, although the relaxation time will be different for different attack angle choices. Different attack angles induce different drag coefficients  $C_D$  and, therefore, kinetic energy is dispersed at different rates.

In Fig. 8(a), the relaxation time as a function of time for the simulations in Figs. 6 and 7 is shown. For the lower atmosphere,

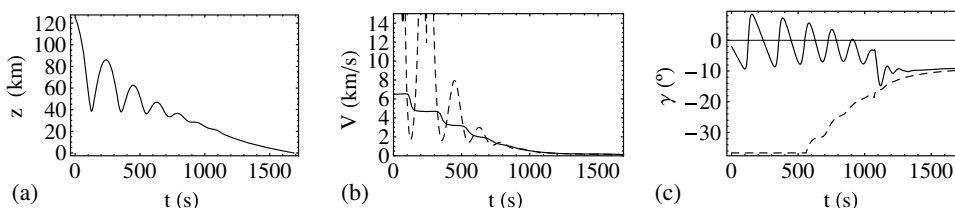


**Fig. 6.** (a) Vertical trajectory of the Space Shuttle in the Earth's atmosphere as a function of time, calculated through Eq. (4), with the attack angle choice  $\alpha = \alpha_{\max gl}$  and the bank angle choice  $\mu = 0$ ; (b–c) glider speed and the flight path descent angle are shown; dotted lines represent the steady states values  $V^*$  and  $\gamma^*$

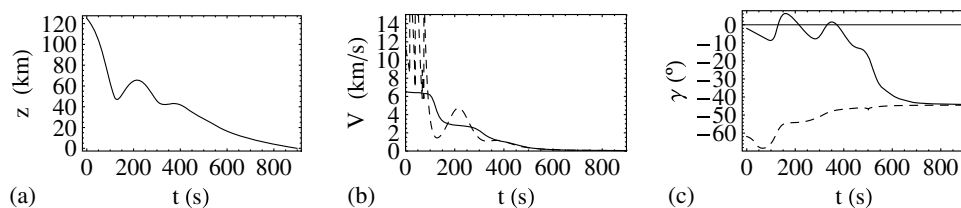


**Fig. 7.** (a) Vertical trajectory of the Space Shuttle in the Earth's atmosphere as a function of time, calculated through Eq. (4), with  $\alpha = \alpha_{\max}$  and  $\mu = 0$ ; (b and c) glider speed and the flight path angle are shown; dotted lines represent the steady states values  $V^*$  and  $\gamma^*$

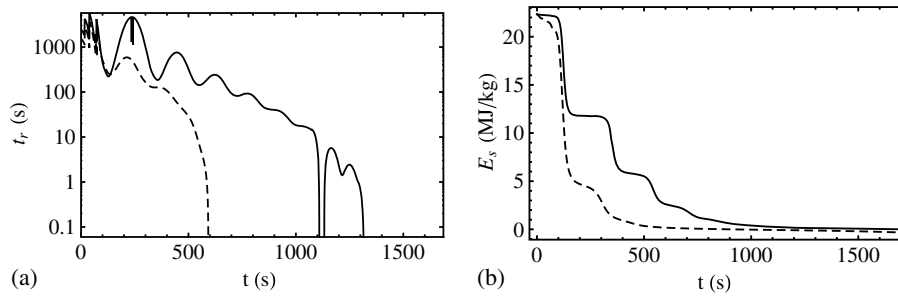


**Fig. 8.** (a) Relaxation times  $t_r$  as a function of time, calculated from Eq. (11), for the simulations presented in Figs. 7 and 6; dotted curve is for the choice  $\alpha = \alpha_{\text{Max}} = 45^\circ$  and the continuous curve is for the choice  $\alpha = \alpha_{\text{maxgl}}$ ; (b) specific energy calculated from Eq. (15)

the relaxation time becomes of the order of a few seconds, implying that algorithms based on the steady state approach work increasingly well as the air density increases.

The specific energy of the glider is given by

$$E_s = \frac{1}{2} V^2 + \int_0^z g(s) ds = \frac{1}{2} V^2 + g_0 \frac{z R_E}{R_E + z} \quad (15)$$

where  $R_E$  = Earth mean radius; and  $g_0$  = Earth gravitational acceleration constant. In Fig. 8(b), the evolution of the specific energy for  $\alpha = \alpha_{\text{maxgl}}$  and  $\alpha = \alpha_{\text{Max}} = 45^\circ$  is shown. From the simulations, it is clear that the choice  $\alpha = \alpha_{\text{Max}}$  dissipates energy faster and stabilizes the flight descent path angle faster than the choice  $\alpha = \alpha_{\text{maxgl}}$ .

The simulations shown in this section should be treated as illustrative, since the parameterizations being used for the aerodynamic coefficients were derived using wind tunnel data valid up to 5 Ma (Ramsey 1972). In the upper layers of the atmosphere, the Space Shuttle travels at higher speeds and the parameterizations derived do not accurately describe its aerodynamic coefficients. Nonetheless, the qualitative behavior of the evolution of the relaxation time and the conclusion that the higher attack angles dissipate energy faster still holds with extended aerodynamic coefficients of Eqs. (12) and (13), covering higher Mach numbers.

## Structural Limits of the Space Shuttle

Any guidance algorithm for a glider traveling in extreme conditions should be designed in such a way that control decisions do not force its structural limits. During maneuvering decisions, three main structural limits have to be considered:

1. Heat flux limit: computed at the Shuttle nose, the most exposed element to heat flux.
2. Load factor limit: computed at the Space Shuttle wings, the most exposed element to load.
3. Acceleration limit: computed inside the Space Shuttle hull.

The heat flux limit imposes a minimum attack angle, while the load factor limit imposes a maximum attack angle. The acceleration limit is related to the maximum acceleration that humans, cargo and electronics can sustain.

### Heat Flux Limit

The Space Shuttle nose is the surface with the lowest curvature radius, thus a limiting factor for the heat flux. In the worst-case scenario hypothesis, the heat flux on the nose of the Space Shuttle is the same as the convective heat flux  $\Phi$  in a laminar flow at a stagnation point ( $V = 0$ ). Under this condition, the heat flux at the Space Shuttle nose is given by (Gallais 2007)

$$\Phi_{\text{nose}} = \Phi \cos \alpha = c_q \sqrt{\frac{\rho(z)}{R_N}} V^3 \cos \alpha \leq \Phi_{\text{Max}} \quad (16)$$

where  $R_N$  = radius of curvature of the Space Shuttle wall;  $\rho(z)$  = density of the atmosphere;  $V$  = speed of the glider;  $\alpha$  = angle of attack; and  $c_q = 1.83 \times 10^{-4} \text{ kg}^{1/2} \text{ m}^{-1}$  = heat conductivity for the Earth atmosphere. Typical values for the Space Shuttle are  $R_N = 1 \text{ m}$  and  $\Phi_{\text{Max}} = 5 \times 10^5 \text{ J/(m}^2\text{s)}$ . The approximation of Eq. (16) is realistic during supersonic flight, where the heat flow to the glider fuselage is mostly laminar. Heat flux becomes relevant typically far above Mach 2.

### Load Factor Limit

For a nonleveled flight with turns, both lift and drag forces have projections orthogonal to the wings, inducing a load on the wings of the glider. This is described by the load factor ( $n_{\text{load}}$ ), usually presented as a multiple of the glider weight (Horneman 2010; Raymer 2006)

$$n_{\text{load}} = \frac{\rho(z) V^2 S}{2 m g(z) \cos(\mu)} [C_L(\alpha, M) \cos \alpha + C_D(\alpha, M) \sin \alpha] \leq n_{\text{max load}} \quad (17)$$

where  $n_{\text{max load}}$  = maximum load factor acceptable at the wings. Typically, the maximum load factor for the Space Shuttle wings is around 4 to 5 times its weight,  $n_{\text{max load}} = 5$ . From the behavior depicted in Fig. 4(a), both the lift and drag coefficients increase with increasing attack angle and thus the angle that induces the biggest wing load is the maximum allowed angle of attack ( $\alpha_{\text{Max}}$ ) when coupled with the maximum allowed bank angle ( $\mu_{\text{Max}}$ ).

### Acceleration Limit

The acceleration limit  $N_g$  is typically measured as a multiple of the gravity acceleration at sea level

$$|N_g| = \left| \frac{\dot{V}}{g(z=0)} \right| \leq g_{\text{lim}} \quad (18)$$

where  $g_{\text{lim}}$  = maximum acceleration limit chosen. Typically, for the Space Shuttle,  $g_{\text{lim}} = 3$ .

## Dynamic Guidance

To control the glider during the atmospheric reentry and during the gliding phase, two types of controls are used to change the

aerodynamic forces and guide the vehicle: the bank angle and the attack angle (Camara 2003). During the early stages of the atmospheric reentry, the effect of the atmosphere is negligible and the motion is governed by the Kepler laws. As the air density increases, the gliding phase is achieved and the aerodynamic forces become strong enough to guide and control the glider.

The usage of a dynamic algorithm that only needs local information as input allows for an autocorrective behavior capable of adapting to variations in the initial conditions and in the atmospheric profiles of air density and temperature. To decide the controls that will be applied iteratively during flight, the guidance algorithm proposed in this paper only requires the input of the glider position, attitude, speed, and atmospheric conditions. In addition, the algorithm also allows for on-board deployment without using preprogrammed maneuvers.

The command and control problem starts with the knowledge of the initial conditions of the glider, both in position and attitude

$$(x_0, y_0, z_0, V_0, \gamma_0, \chi_0)$$

corresponding, without loss of generality, to the starting control time  $t_0 = 0$ . The spatial coordinates of the target point are

$$(x_f, y_f, z_f)$$

By definition, the *handover sphere* is a spherical region centered at  $(x_f, y_f, z_f)$ , with radius  $r_{\text{target}}$ .

The intermediate coordinates and attitude parameters of the glider trajectory are

$$(x_i, y_i, z_i, V_i, \gamma_i, \chi_i),$$

where  $i = 0, 1, \dots, f$ . These intermediate coordinates are measured at time  $t_i = iT_{\text{con}}$ , where  $T_{\text{con}}$  is the control time interval that measures the time interval between two successive control commands.

In the configuration space  $(x, y, z)$ , the direction vector from the actual position  $(x_i, y_i, z_i)$  to the target point is

$$\vec{P}_i = (x_f - x_i, y_f - y_i, z_f - z_i) \quad (19)$$

The attack and bank angles are controlled separately at each time step  $t_i$  of the dynamic control process. At each time step  $t_i$ , the initial conditions are  $(x_i, y_i, z_i, V_i, \gamma_i, \chi_i)$  and the glider commands are  $(\mu_i, \alpha_i)$ . At  $t_i$ , a set of new commands  $\alpha_{i+1}$  and  $\mu_{i+1}$  are recalculated. During the time interval  $(t_i, t_{i+1}]$ , the glider will have the control values  $(\mu_{i+1}, \alpha_{i+1})$ , defined according to the five steps of the dynamic guidance algorithm.

The algorithm stops when the target altitude is reached. At that instant, the distance to the target or error distance  $e_d$  is measured.

In (Dilão and Fonseca 2013), a reduced form of the algorithm has been tested using only the navigations components of the algorithm proposed here—steps (1) and (3) from the algorithm proposed in this paper.

### Dynamic Guidance Algorithm

The dynamic guidance algorithm is divided into five steps:

1. Bank angle navigation control: bank angle needed to reach the target.
2. Bank angle energy control: bank angle needed to avoid climbing due to excessive kinetic energy.
3. Attack angle navigation control: attack angle needed to reach the target.
4. Attack angle load factor control: maximum attack angle to prevent excessive load at the wings.

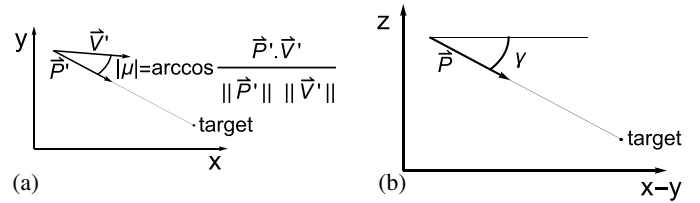


**Fig. 9.** Geometric construction of (a) the bank angle navigation control and of (b) the attack angle navigation control; the axis where the  $(x, y)$  plane intersects the vertical plane that contains the vector  $\vec{P}$  is indicated by “ $x-y$ ”

5. Attack angle heat flux control: minimum attack angle to prevent excessive heat flux at the nose.

### Bank Angle Navigation Control

The bank angle navigation control guides the glider in the  $(x, y)$  plane, by correcting the angular misalignment between  $\vec{P}_i$  and the current speed  $\vec{V}_i$ . From the geometric construction in Fig. 9(a), the correct alignment angle is

$$\begin{aligned} \mu_{i+1}^{\text{navigation}} &= -\arccos \frac{\vec{P}_i' \cdot \vec{V}_i'}{\|\vec{P}_i'\| \|\vec{V}_i'\|} \text{Sign}[(\vec{P}_i \wedge \vec{V}_i)_z] \\ &= -\arccos \left[ \frac{P_{ix} V_{iy} + P_{iy} V_{ix}}{\sqrt{(P_{ix}^2 + P_{iy}^2)(V_{ix}^2 + V_{iy}^2)}} \right] \\ &\quad \times \text{Sign}(P_{ix} V_{iy} - P_{iy} V_{ix}) \end{aligned} \quad (20)$$

provided that  $\mu_{i+1}^{\text{navigation}} \in [-\mu_{\text{Max}}, \mu_{\text{Max}}]$ , where  $\mu_{\text{Max}}$  = maximum allowed bank angle for the glider maneuvering. If  $|\mu_{i+1}^{\text{navigation}}| > \mu_{\text{Max}}$ , the choice made is  $|\mu_{i+1}^{\text{navigation}}| = \mu_{\text{Max}}$ . The Sign function is defined as  $\text{Sign}(P_{ix} V_{iy} - P_{iy} V_{ix}) = 1$  if  $P_{ix} V_{iy} - P_{iy} V_{ix} \geq 0$ , and  $\text{Sign}(P_{ix} V_{iy} - P_{iy} V_{ix}) = -1$  otherwise. As usual, the dot refers to the scalar product and the caret to the vector product. The vectors  $\vec{P}_i'$  and  $\vec{V}_i'$  are the projections of  $\vec{P}_i$  and  $\vec{V}_i$  in the  $(x, y)$  plane.

### Bank Angle Energy Control

This control is introduced to prevent transients with sharp climbs and dives, by performing dynamic S-turns when the glider is traveling far above the steady state speed. The bank angle energy control is

$$\mu_{i+1}^{\text{energy}} = \mu' \cdot \text{Sign}\{\sin[2\pi f_{\text{energy}}(t_i - t_{i0} + T_{\text{con}}) + \phi_0]\} \quad (21)$$

where  $\mu_{i+1}^{\text{energy}} \in [-\mu_{\text{Max}}, \mu_{\text{Max}}]$ . At each control time  $t_i$ , the following conditions are evaluated:

- Is the current flight descent-path angle positive ( $\gamma > 0$ )?
- Is the current speed above the maximum steady-state speed,  $V_i > V_{(\alpha_i=\alpha_{nl}, \mu_i=\mu_{\text{Max}})}^*$ ?
- Is the current speed above the critical supersonic threshold,  $M_i > M_c$ ?

If the three previous conditions are met simultaneously, the glider is climbing due to excessive kinetic energy. Avoiding additional climbing is equivalent to computing the bank angle that satisfies the condition  $\dot{\gamma} = 0$ . Thus

$$\mu' = \begin{cases} \arccos \left[ \frac{2 \, mg(z_i) \cos \gamma_i}{S \rho(z_i) C_L(\alpha_i, Ma_i) V_i^2} \right] & \text{if } a, b, \text{ and } c \text{ are true} \\ 0 & \text{otherwise} \end{cases}$$

Finally, the periodic modulation component is computed based on

$$\phi_0 = \begin{cases} 0 & \text{if } \text{Sign}(\mu_i^{\text{navigation}}) \cdot \text{Sign}\{\sin[2\pi f_{\text{energy}}(t_i - t_{i0} + T_{\text{con}})]\} \geq 0 \\ \pi & \text{if } \text{Sign}(\mu_i^{\text{navigation}}) \cdot \text{Sign}\{\sin[2\pi f_{\text{energy}}(t_i - t_{i0} + T_{\text{con}})]\} = -1 \end{cases}$$

where  $f_{\text{energy}}$  is a low-frequency parameter defining how fast the S-turn maneuver is performed and  $t_{i0}$  is the instant where the S-turn maneuver is initiated.

### Final Bank Angle Control

With the controls just enumerated, the final bank angle control can be calculated. Defining

$$\mu_{i+1}^{\text{value}} = \max\{|\mu_{i+1}^{\text{navigation}}|, |\mu_{i+1}^{\text{energy}}|\}$$

and

$$\mu_{i+1}^{\text{sign}} = \begin{cases} \text{Sign}(\mu_{i+1}^{\text{energy}}) & \text{if } |\mu_{i+1}^{\text{energy}}| > |\mu_{i+1}^{\text{Max}}| \\ \text{Sign}(\mu_{i+1}^{\text{navigation}}) & \text{otherwise} \end{cases}$$

the final bank angle control is

$$\mu_{i+1} = \min\{\mu_{i+1}^{\text{value}}, \mu_{\text{Max}}\} \cdot \mu_{i+1}^{\text{sign}} \quad (22)$$

### Attack Angle Navigation Control

The attack angle navigation control corrects the vertical orientation of the glider to the target through a straight line path, as depicted in Fig. 9(b). The tangent of the descent path angle that points from the current position  $(x_i, y_i, z_i)$  to the target position is

$$G_{i+1} = \frac{(z_f - z_i)}{\sqrt{(x_f - x_i)^2 + (y_f - y_i)^2}} \quad (23)$$

At time  $t = t_i$ , the glider has a flight descent path angle  $\gamma_i$  that needs to converge to  $\arctan(G_{i+1})$ . So, by Eq. (5)

$$G_{i+1} = (\tan \gamma_{i+1}) = -\frac{C_D(\alpha_{i+1}, M_i)}{C_L(\alpha_{i+1}, M_i) \cos \mu_{i+1}^{\text{navigation}}} \quad (24)$$

With the calculated value of  $G_{i+1}$ , Eq. (23), and solving Eq. (24) in order to the ratio  $C_L/C_D$ , in the range  $\alpha_{i+1} \in [\alpha_{\text{maxgl}}, \alpha_{\text{Max}}]$ , three cases may occur

- If  $G_{i+1} \cos \mu_{i+1}^{\text{navigation}} > C_L(\alpha_{\text{maxgl}}, M_i)/C_D(\alpha_{\text{maxgl}}, M_i)$ , then,  $\alpha_{i+1}^{\text{navigation}} = \alpha_{\text{maxgl}}$ ;
- If  $G_{i+1} \cos \mu_{i+1}^{\text{navigation}} < C_L(\alpha_{\text{Max}}, M_i)/C_D(\alpha_{\text{Max}}, M_i)$ , then,  $\alpha_{i+1}^{\text{navigation}} = \alpha_{\text{Max}}$ ;
- Otherwise,  $G_{i+1} \cos \mu_{i+1}^{\text{navigation}} = C_L(\alpha_{i+1}, M_i)/C_D(\alpha_{i+1}, M_i)$  is numerically solved to determine  $\alpha_{i+1}$  with a precision  $\alpha_{\text{precision}}$ .

The  $C_L/C_D$  curve as a function of  $\alpha$  and Mach number  $M$  is given by Eqs. (12) and (13). The  $\alpha_{\text{maxgl}}$  is calculated from Eq. (14) and the Mach number is computed using Eq. (3).

### Attack Angle Load Factor Control

The load constraint Eq. (17) at the glider wings is checked

$$n_{\text{load}_{i+1}} = \frac{\rho(z_i) V_i^2 S}{2mg(z_i) \cos(\mu_{i+1})} [C_L(\alpha_{i+1}, M_i) \cos \alpha_{i+1} + C_D(\alpha_{i+1}, M_i) \sin \alpha_{i+1}] \leq n_{\text{max load}} \quad (25)$$

If this condition is violated, the angle of attack will be recalculated by numerically solving  $n_{\text{load}_{i+1}} = n_{\text{max load}}$  with a precision

$\alpha_{\text{precision}}$  in the range  $\alpha_{i+1}^{\text{load}} \in [\alpha_{nl}, \alpha_{\text{Max}}]$ . The  $\alpha$  solution in the interval  $\alpha_{i+1}^{\text{load}} \in [\alpha_{nl}, \alpha_{\text{maxgl}}]$  has both less lift and less drag, as shown in Fig. 4(a).

### Attack Angle Heat Flux Control

In this control, it is checked if the heat flux constraint Eq. (16) is violated at the glider nose

$$c_q \sqrt{\frac{\rho(z_i)}{R_N}} V_i^3 \cos(\alpha_{i+1}) \leq \Phi_{\text{Max}} \quad (26)$$

If the inequality of Eq. (26) does not hold,  $\alpha_{i+1}^{\text{heat}}$  is computed in the range  $\alpha_{i+1}^{\text{heat}} \in [\alpha_{nl}, \alpha_{\text{Max}}]$  by solving

$$\alpha_{i+1}^{\text{heat}} = \arccos \left[ \Phi_{\text{Max}} \frac{1}{c_q V_i^3} \sqrt{\frac{R_N}{\rho(z_i)}} \right] \quad (27)$$

### Final Attack Angle Control

The final attack angle control  $\alpha_{i+1}$  is given by

$$\alpha_{i+1} = \text{Max}[\text{Min}(\alpha_{i+1}^{\text{navigation}}, \alpha_{i+1}^{\text{load}}), \alpha_{i+1}^{\text{heat}}]$$

The controls are recalculated at each instant of time  $t = t_i$  until the target height is reached. To prevent abrupt maneuvers near the target, inside the handover sphere, the bank angle is set to zero and the attack angle is locked to  $\alpha_{\text{Max}}$ .

## Simulations

The trajectory of the glider will be calculated with Eq. (4), using a fourth-order Runge-Kutta integration method with an integration time step  $T_{\text{int}}$ , where  $nT_{\text{int}} = T_{\text{con}}$  and  $n$  is a positive integer. The planetary atmosphere parameters are described in detail in Dilão and Fonseca (2013).

Using data from Findlay et al. (1982) and Rehder and Holloway (1972) for testing, the following parameters have been chosen:

- Glider initial conditions (Space Shuttle)
 
$$(x_0, y_0, z_0) = (0, 0, 30,000 \text{ m}),$$

$$V_0 = 1,100 \text{ m/s} (= 3.65 \text{ M}), \quad \mu_0 = 0^\circ,$$

$$\alpha_0 = 30^\circ, \quad \gamma_0 = -3^\circ, \quad \chi_0 = 0^\circ \quad (28)$$

- Parameters and physical constraints of the glider (Space Shuttle)

$$S = 299.9 \text{ m}^2, \quad m = 82,500 \text{ kg}, \quad \alpha_{nl} = 1.5^\circ,$$

$$\alpha_{\text{max}} = 45^\circ, \quad \mu_{\text{max}} = 60^\circ, \quad \Phi_{\text{max}} = 5 \times 10^5 \text{ W/m}^2,$$

$$n_{\text{max load}} = 5, \quad g_{\text{lim}} = 3 \quad (29)$$

- Guidance algorithm parameters

$$T_{\text{con}} = 0.1 \text{ s}, \quad T_{\text{int}} = 0.1 \text{ s}, \quad r_{\text{target}} = 100 \text{ m},$$

$$\alpha_{\text{precision}} = 0.0573^\circ, \quad f_{\text{energy}} = 1/60 \text{ Hz} \quad (30)$$

- Target coordinates (HAC center)

$$(x_f, y_f, z_f) = (x_f, y_f, 3,000 \text{ m}) \quad (31)$$



The goal of the guidance algorithm is to conduct the glider to the target point at the center of the HAC. The maximum range of the glider under the control of this algorithm will be analysed first. Then, a typical trajectory of the guidance algorithm will be generated. Finally, a sensitivity analysis for variations of the initial conditions, of the time control interval and of the atmospheric profiles of air density and temperature will be performed. As the wind tunnel data from Ramsey (1972), used to derive the aerodynamic coefficients, only covered speeds up to 5 M, the simulation are initiated at the altitude of 30 km, where the glider speed is typically well within that range. Nonetheless, the algorithm is applicable to higher heights and speeds without any intrinsic restrictions.

### Glider Range at the Target Altitude

With initial conditions of Eq. (28), for straight-line flights [ $\mu = 0$  implies  $y(t) = y_0$  for  $t \geq 0$ ], the maximum range is achieved with attack angles  $\alpha = \alpha_{\max gl}$ , Fig. 10(a). The minimum range in straight-line flights is obtained with the choice  $\alpha = \alpha_{\max}$ , Fig. 10(a). From the simulations presented in Fig. 10(a) for straight-line flights, the smaller range is  $x_{sr} = 76,467$  m and the maximum range is  $x_{mr} = 270,462$  m, with flight times 403.1 s and 725.3 s, respectively.

For flights not restricted to an  $(x, z)$  vertical plane ( $\mu \neq 0$ ), the target coordinates  $(x_f, y_f)$  were located in a two-dimensional circular domain at the altitude  $z_f = 3,000$  m, outside the accessible region. These target coordinates force the algorithm to always select the attack angle  $\alpha_{\max gl}$ . In Fig. 10(b), the two-dimensional maximum range curve  $R_{\max gl}$  is shown. The range achieved when traveling at maximum attack angle  $\alpha = \alpha_{\max}$  is marked  $R_{\max}$  in Fig. 10(b).

From these simulations, it follows that for initial velocities misaligned with the direction from the current position to the target point lead to a marked decrease in the range of the glider. This is a consequence of the poor maneuvering response of the glider at high altitudes.

### Dynamic Guidance Trajectories

From the analysis of the maximum range of the glider, the following target coordinates have been chosen

$$(x_f, y_f, z_f) = (180,000 \text{ m}, 90,000 \text{ m}, 3,000 \text{ m}) \quad (32)$$

and were indicated by the letter  $T$  in Fig. 10(b).

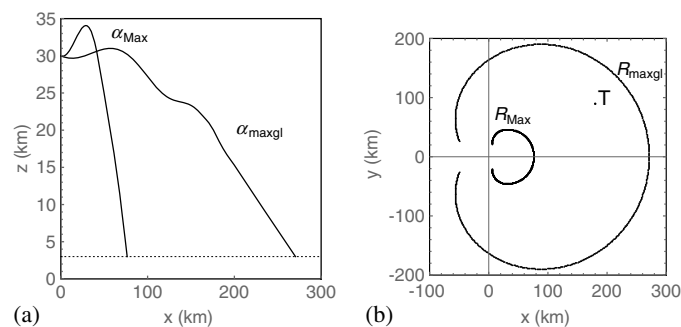


**Fig. 10.** (a) Maximal and minimal range trajectories for a Space Shuttle flight with  $y(t) = 0$  and the reference conditions of Eqs. (28)–(29) and (31); (b) maximum range curve ( $R_{\max gl}$ ) and the range curve at maximum attack angle ( $R_{\max}$ ) in the  $(x, y)$  plane, at  $z_f = 3,000$  m;  $T$  is the position of the target coordinates as in Eq. (32)

The three-dimensional dynamically controlled trajectory obtained with the guidance algorithm is shown in Fig. 11, for the reference conditions of Eqs. (28)–(30) and (32). Across the entire flight, the command history decided by the algorithm varies slowly, and thus the dynamic trajectory of the glider is smooth. The time of arrival at the target is  $t = 614.5$  s, the final speed is  $V_f = 62.6$  m/s, and the distance error is  $e_d = 21.2$  m.

When the algorithm takes control of the flight, the glider is traveling at a supersonic speed and the  $L/D$  ratio is quite small, making the HAC seems to be nonachievable, Fig. 11(e). In this region, the algorithm responds by imposing the angle of attack  $\alpha_{\max gl}$ . As the glider loses speed and the aerodynamic balance of the  $L/D$  ratio improves, the  $L/D$  ratio enters the accessible region delimited by the aerodynamic limits defined between the attack angles  $\alpha_{\max gl}$  and  $\alpha_{\max}$ . At this time, the algorithm responds by correctly selecting the attack angles that delivers the glider to the target.

### Sensitivity to the Control Time Interval

To evaluate the algorithm sensitivity to changes in the control time interval, we have changed  $T_{\text{con}}$  in the interval  $[0.1 \text{ s}, 35 \text{ s}]$  for the same target coordinates of Eq. (32) and the same reference conditions of Eqs. (28)–(30) and (32). In Fig. 12(a), several trajectories computed with the different control time intervals are shown, as well as the overall distance error at the end of each run, as a function of  $T_{\text{con}}$ , Fig. 12(b). For small control time intervals, the distance error  $e_d$  increases linearly and slowly as a function of  $T_{\text{con}}$ , and  $20 \leq e_d \leq 80$  m, for  $0.1 \leq T_{\text{con}} \leq 30$  s. In the lower layers of

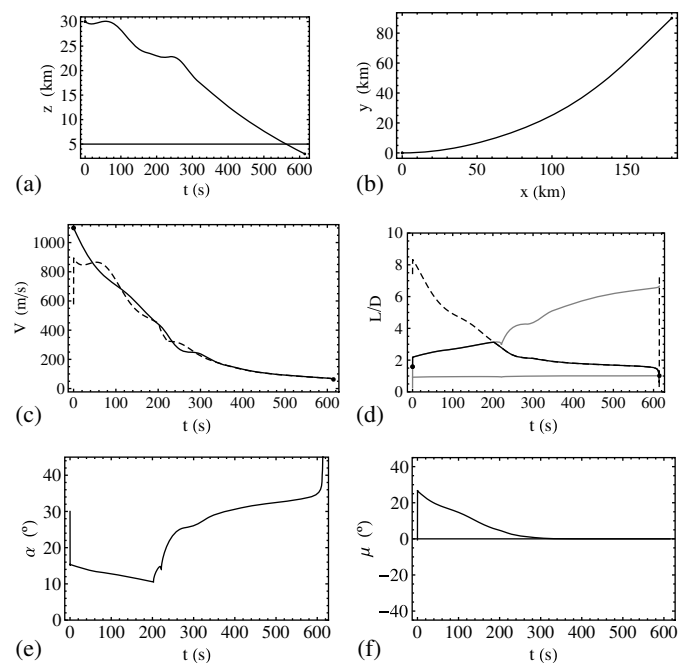


**Fig. 11.** Dynamic guidance trajectory of a glider (Space Shuttle): (a) time evolution of the altitude of the glider; (b) projection of the dynamically controlled trajectory in the  $(x, y)$  horizontal plane; (c) speed and the steady state speed (dashed) as a function of time; (d) time evolution of the lift over drag ratio  $L/D$  is shown; grey lines represent the aerodynamic limits of flying either with attack angle at max-range or at the maximum attack angle; dashed line is the  $L/D$  ratio needed to achieve the target in a straight-line path at each control time, and the full line is the decision made by the algorithm; (e and f) time sequence of controls made by the algorithm

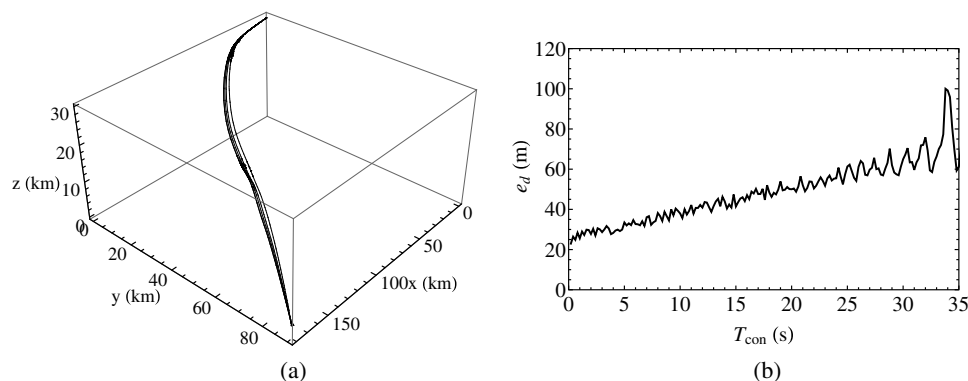


**Fig. 12.** (a) Dynamic guidance trajectories in space for  $T_{\text{con}} = 0.1, 1, 10, 20, 40$  s and reference conditions Eqs. (28)–(30) and (32); (b) error distance to the target as a function of the control time interval  $T_{\text{con}}$

the atmosphere, the different trajectories converge as they approach the target.

### Sensitivity to the Initial Conditions

To measure the sensitivity of the control algorithm to changes in the initial conditions, the four initial conditions  $\gamma_0$ ,  $\chi_0$ ,  $z_0$ , and  $V_0$  have been changed independently, keeping the target coordinates constant.

The variations of the error distances at the end of each run are shown in Fig. 13. From Figs. 13(a and b), it is clear that, in the horizontal plane ( $x, y$ ), there is a wide window of acceptable initial misalignments with the target direction in both  $\chi_0$  and  $\gamma_0$ . From Figs. 13(c and d), it can be concluded that the algorithm also has a wide window of possible initial conditions for both the initial height and the initial speed. Therefore, we conclude that the algorithm is resilient to changes in  $\gamma_0$ ,  $\chi_0$ ,  $z_0$ , and  $V_0$ .

The impact of different initial speeds on the structural limits of the glider has been analyzed by massively increasing the initial speed relatively to the reference initial speed ( $V_0 = 1,100$  m/s).

As shown in Fig. 14, the algorithm kept both the wing load and the heat flux at the nose below the structural limits.

In Fig. 14(a), the heat flux at the Space Shuttle nose is computed [Eq. (16)]. The control acted only for a brief moment to ensure  $\Phi_{\text{Max}}$  was not exceeded for the highest initial speed. In Fig. 14(b), the load at the Space Shuttle wings is depicted, Eq. (17), where, for the two highest initial speeds, the attack angle load limit control intervened to maintain the maximum wing load, according to existing structural limit  $n_{\text{Max}}$ . The biggest strain on the wings occurs when there is a conjugation of high speeds, high attack angles, and high bank angles. In Fig. 14(c), the acceleration inside the Space Shuttle is calculated [Eq. (18)]. The most negative accelerations are obtained for the highest initial speeds and the typical maximum admissible acceleration ( $g_{\text{lim}} = 3$ ) is violated only during a short period of time.

Although these extreme initial conditions are unlikely to happen, the energy and load analysis were included in the algorithm to improve its resilience in a wide range of situations. This includes emergency situations where, for example, a severe problem occurred in the reentry burn and the Space Shuttle did not decelerate enough before entering the atmosphere.

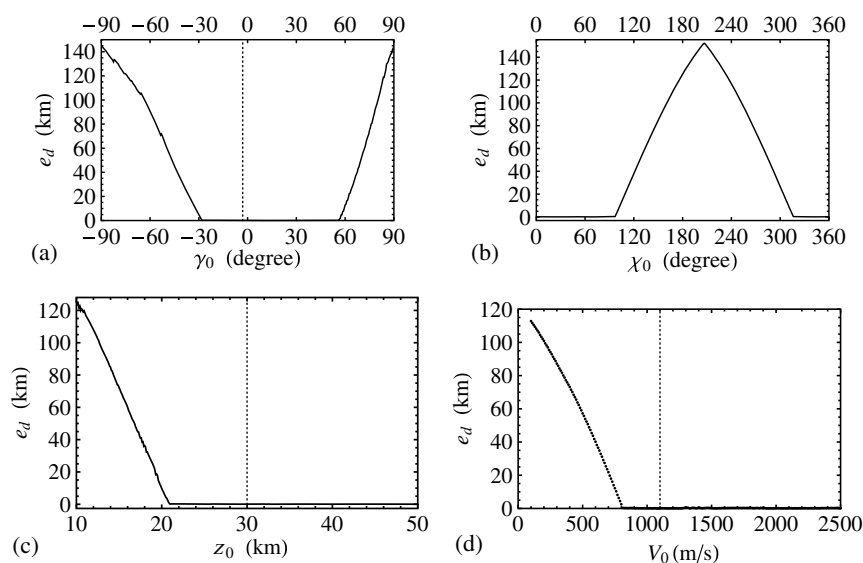


**Fig. 13.** Variation of the distance errors to the target point [Eq. (32)] for different initial conditions in (a)  $\gamma_0$ ; (b)  $\chi_0$ ; (c)  $z_0$ ; (d)  $V_0$ ; reference initial conditions of Eq. (28) are marked by the dotted line

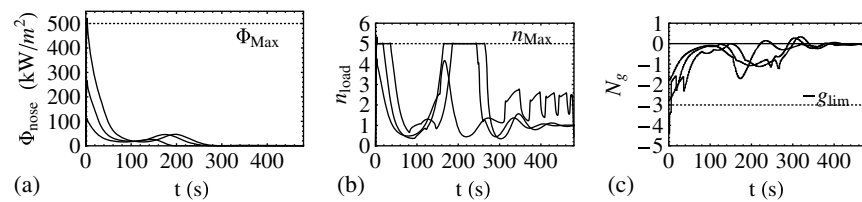


**Fig. 14.** Time variation of the glider structural parameters (a)  $\Phi_{\text{nose}}$ ; (b)  $n_{\text{load}}$ ; (c)  $N_g$ , for the initial speeds  $V_0 = 1100, 1650, 2200$  and  $2,750$  m/s; dotted lines represent the structural limits of the Space Shuttle

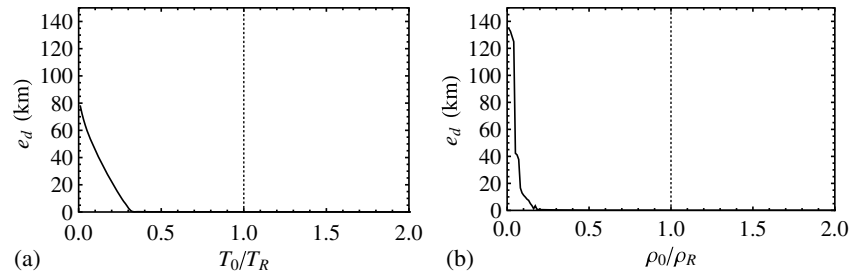


**Fig. 15.** Variation of the distance errors to the target point [Eq. (32)], for changes in the expected atmospheric profile for (a) temperature and (b) density; reference initial conditions  $T_0$  and  $\rho_0$  are marked by the dotted line; atmospheric profiles were scaled by a constant varying from 0.1 to 1.99

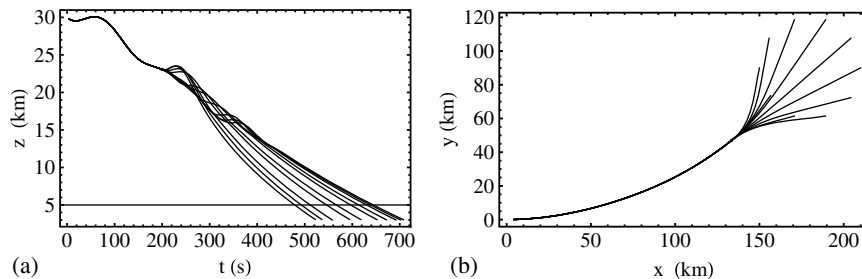


**Fig. 16.** In-flight trajectory reprogramming; at  $t = 200$  s, the target was changed to new locations: (a) time evolution of the glider trajectory as a function of the altitude  $z$ ; (b) different trajectories in the  $(x, y)$  plane

### Sensitivity to Atmospheric Profile Changes

To test the resilience of the algorithm to atmospheric changes, separate simulations were performed with altered atmospheric profiles of air density and air temperature. By Eq. (3), the local temperature affects the Mach number. In these simulations, the entire atmospheric profiles were multiplied by a constant. The results are shown in Fig. 15. From these simulations it is possible to conclude that, unless air density or air temperature is less than half of what was expected, there will be no relevant impact in the error distance at the end of each run.

### Flexibility to Change the Target Position during Flight

Flexibility is important to deal with situations where there is a need to change the target position during flight. This can occur, for example, in emergency situations where there is a sudden storm over the runway. To illustrate the flexibility of the algorithm, several simulations were ran and the target was changed to a new location at  $t = 200$  s. At that instant of time, the algorithm started receiving a new set of coordinates for the final target and adjusted

accordingly. The results of the trajectory reprogramming is shown in Fig. 16, showing the flexibility of the algorithm for target redefinition.

### Conclusions

A new guidance algorithm to automate the flight of a glider maneuvering in a planetary atmosphere has been proposed and tested. The algorithm dynamically decides the bank and attack angle controls using the local position, the current attitude, and the relative position of the target. The algorithm has been tested in a simulated Space Shuttle automatic flight starting at approximately 200 km from the target, at the altitude of 30 km, where the Earth atmospheric density becomes significant enough to enable the use of aerodynamic forces to control the glider.

The proposed guidance algorithm successfully delivered the Space Shuttle to the target with distance errors in the range of 20–80 m, with control time intervals from 0.1 to 30 s. The algorithm dynamically manages the controls without violating the

structural limits of the Space Shuttle. This has been checked, both in terms of the maximum heat flux at the nose and the maximum load at the wings, even in extreme situations that are not likely to occur, such as extreme initial speeds after a severe problem in the reentry burn.

The algorithm proved to be extremely resilient to changes in the initial conditions in terms of the initial altitude, the initial speed, the initial flight descent path angle, and the initial orientation in the  $(x, y)$  plane. The algorithm also presents strong resilience to variations in the time control interval and in the atmospheric profiles of air density and temperature. Additionally, the algorithm has shown extreme flexibility to changes in the final target while in flight. Applying the algorithm to any other glider is straightforward, and can be done by adapting the aerodynamic coefficients and the structural limits to reflect the characteristics of the new glider.

From the computational point of view, this guidance algorithm is not computationally demanding, depending on the local information of position, attitude, and speed and on an onboard numerical integrator of the trajectory, compatible with the fitted aerodynamic characteristics of glider. As the guidance system proposed here depends mainly on the current state of the glider, errors do not accumulate from one step to the next.

## Acknowledgments

The authors wish to thank the constructive comments of the referees of this paper.

## References

- Betts, J. T. (1998). "Survey of numerical methods for trajectory optimization." *J. Guid. Control Dyn.*, 21(2), 193–207.
- Betts, J. T. (2010). "Practical methods for optimal control and estimation using nonlinear programming." *Advances in design and control*, 2nd Ed., Vol. 19, SIAM, Philadelphia, 247–293.
- Bonnard, B., Faubourg, L., and Trélat, E. (2005). "Optimal control of the atmospheric arc of a space shuttle and numerical simulations by multiple-shooting techniques." *Math. Models Methods Applied Sci.*, 15(1), 109–140.
- Câmara, F. M. C. (2003). "Development and design of the terminal area energy management guidance for a reusable launch vehicle." Master thesis, Delft Univ. of Technology, Astrium, Delft, Netherlands.
- Costa, R. R. (2003). "Studies for terminal area GNC of reusable launch vehicles." *AIAA Guidance, Navigation, and Control Conf. and Exhibit*, AIAA 2003-5438, Austin, TX.
- Dilão, R., and Fonseca, J. (2013). "Dynamic trajectory control of gliders." *Advances in Aerospace Guidance, Navigation and Control, Selected Papers of the 2nd CEAS Specialist Conf. on Guidance, Navigation and Control*, Q. Chu, B. Mulder, D. Choukroun, E. van Kampen, C. Visser, and G. Looye, eds., Springer, Berlin, 373–386.
- Findlay, J. T., Kelly, G. M., and Heck, M. L. (1982). "Reconstruction of the 1st Space Shuttle (STS-1) Entry Trajectory." *NASA Contractor Rep. 3561*, Washington, DC.
- Gallais, P. (2007). *Atmospheric re-entry vehicle mechanics*, Vol. 151, Springer, Berlin, 31–33.
- Harpold, J., and Gavert, D. (1983). "Space shuttle entry guidance performance results." *J. Guidance*, 6(6), 442–447.
- Harpold, J., and Graves, C. (1979). "Shuttle entry guidance." *NASA-TM-79949, JSC-14694*, Lyndon B. Johnson Space Center, Houston.
- Horneman, K. (2010). *Automated trajectory generation and guidance for a new launch vehicle flight phases*, Faculty of the Graduate School, Univ. of Missouri-Columbia, Columbia, MO.
- Hull, D. G. (2007). *Fundamentals of airplane flight mechanics*, Springer, Berlin, 22–23.
- Jiang, Z., and Ordonez, R. (2007). "Trajectory generation on approach and landing for RLVs using motion primitives and neighboring optimal control." *Proc., 2007 American Control Conf. ACC'07*, IEEE, New York, 1091–1096.
- Lu, P. (2014). "Entry guidance: A unified method." *J. Guidance Control Dyn.*, 37(3), 713–728.
- Mease, K. D., Teufel, P., Schonenberger, H., Chen, D. T., and Bharadwaj, S. (1999). "Re-entry trajectory planning for a reusable launch vehicle." *AIAA Paper 99-4160*, American Institute of Aeronautics and Astronautics, Reston, VA.
- Miele, A. (1962). *Flight mechanics, theory of flight paths*, Addison-Wesley, Reading, MA.
- NASA. (1976). "US standard atmosphere." *NASA-TM-X-74335*, Washington, DC.
- Ramsey, P. E. (1972). *Space shuttle aerodynamic stability, control effectiveness and drag characteristics of a shuttle orbiter at Mach Numbers from 0.6 to 4.96*, NASA/MSFC, Huntsville, AL.
- Raymer, D. P. (2006). *Aircraft design: A conceptual approach*, 4th Ed., American Institute of Aeronautics and Astronautics, Reston, VA, 320.
- Rehder, J. J., and Holloway, P. F. (1972). *Orbiter entry trajectory considerations*, NASA Langley Research Center, Hampton, VA.
- Shevell, R. S. (1988). *Fundamentals of flight*, 2nd Ed., Prentice Hall, Upper Saddle River, NJ, 133.
- Trélat, E. (2003). "Optimal control of a space shuttle and numerical simulations." *Discrete Continuous Dyn. Syst. Ser. S, AIMS*, 842–851.
- Trélat, E. (2012). "Optimal control and applications to aerospace: Some results and challenges." *J. Optim. Theory Appl.*, 154(3), 713–758.
- Vernis, P., and Ferreira, E. (2004). *On-board trajectory planner for the TAEM guidance of a winged-body*, EADS Space Transportation, Paris.
- Zipfel, P. H. (2007). *Modeling and simulation of aerospace vehicle dynamics*, American Institute of Aeronautics and Astronautics, Reston, VA.